

ORIGINAL ARTICLE

Evaluation of rare-earth element dopants (Sm and Er) on ablation resistance of ZrB₂/SiC-sintered billets

Angel A. Peña¹  | Jonathan P. Vernon² | Rodney W. Trice¹¹School of Materials Engineering, Purdue University, West Lafayette, Indiana²Air Force Research Laboratory, W-P AFB, Ohio**Correspondence**Angel A. Peña, School of Materials Engineering, Purdue University, West Lafayette, Indiana.
Email: pena21@purdue.edu**Funding information**

Air Force Office of Scientific Research, Grant/Award Number: FA9550-16-1-0039

Abstract

In this paper, how rare-earth element dopants (samarium and erbium) affect the scale development of sintered ZrB₂/SiC (ZBS) samples during ablation testing was investigated. ZBS billets with five different Sm to Er ratios, with a nominal total amount of 3 mol% dopant incorporated, were prepared by sintering in vacuum to 2000°C and subjected to 60 and 300 seconds ablation cycles. Differences in surface temperatures between ZBS samples with different dopant ratios suggests differences in spectral absorptance/emittance between each of the five compositions investigated. ZBS billets co-doped with Sm and Er form a beneficial c_1 -(Sm/Er)_{0.2}Zr_{0.8}O_{1.9} oxide scale as the majority phase, with some glassy phase observed. The crystalline c_1 -(Sm/Er)_{0.2}Zr_{0.8}O_{1.9} oxide scale is more thermally stable than the m -ZrO₂ oxide scale typically formed in oxidized ZBS systems, resulting in a more adherent oxide scale to the unreacted material. The crystalline oxide scale and the amorphous phase are formed by a convection cell mechanism where the c_1 -(Sm/Er)_{0.2}Zr_{0.8}O_{1.9} crystalline islands precipitate, grow, and coalesce.

KEYWORDS

ablation, erbium, hypersonic, samarium, Zirconia

1 | INTRODUCTION

Hypersonic vehicle design involves the use of sharp leading edges to improve performance and reduce aerodynamic drag.^{1,2} During hypersonic flight, a substantial amount of energy is transferred to the vehicle leading edge by convection and chemical heating.³ Convective heating, caused by the high enthalpy bow shock layer, can result in strong thermal shock in the vehicle's sharp leading edges.¹ The atmospheric friction during the re-entry process causes the diatoms in the air to separate into ions, which in turn, recombine on the hot surface to release energy resulting in chemical heating.⁴ Both processes can heat leading edges to $\geq 2000^\circ\text{C}$.

Among the ultrahigh-temperature ceramics (UHTC) being considered for leading edges, studies have shown that ZrB₂/SiC (ZBS) is a promising material for hypersonic applications due to its high melting point and strength at

1500°C and above, as well as its ablation and thermal shock resistance.³⁻⁶ Despite all of these benefits, ZBS becomes less effective at temperatures above 1600°C due to the evaporation of the protective glassy oxide layers formed by oxidation of the SiC.^{4,7,8} Because of this, finding a means to reduce the surface temperature during hypersonic flight is an urgent issue. Leading edge surface temperatures can be reduced by two ways. A UHTC with a high thermal conductivity is beneficial because it reduces the thermal gradient and the undesirable effects of local hot spots.⁴ A UHTC can also reduce surface temperature via radiation.⁴ The relevant material property is emittance, with a value approaching that of a black body desired. Studies performed by Tan et al.^{3,4,9} have shown that adding Sm dopant to ZBS increases its emittance compared to ceramics comprised of only ZBS. Specifically, a total emittance of 0.9 at 1600°C was measured for a coating with 5 mol% Sm

dopant and a balance of ZrB_2/SiC .⁹ Furthermore, the Sm dopant improved ablation performance by forming a stable oxide scale of $c_7-Sm_{0.2}Zr_{0.9}O_{1.9}$, which has a melting point of 2700°C, and thus can withstand temperature extremes expected during hypersonic flight.⁹

From a scientific standpoint, it would be helpful if emittance could be tailored at different wavelengths. For example, materials with tailorable emittance could be used to improve the efficiency of engines, thermophotovoltaic cells, and other applications.^{9–11} One approach to create a ceramic with tailorable emittance would be to use two different rare-earth elements, adding them to a UHTC in small quantities. In this approach, one rare-earth element is added to increase the emittance of the UHTC over a large wavelength range (visible to near infrared wavelengths, consistent with the temperature range expected for hypersonic flight) and another is added to decrease the emittance at specific wavelength range. The end result is a UHTC, in structural or coating form, with selective emittance. Samarium oxide has been shown to have a high emittance from visible to near IR wavelengths.^{12,13} Erbium oxide has a demonstrated low emittance in several wavelength ranges, specifically in the 0.7–0.8 μm , 1–1.1 μm , and 1.7–1.8 μm ranges.¹³

With this in mind, the goal of this study was to dope a UHTC with two rare-earth elements, employing both samarium and erbium, to evaluate the effects of Sm and Er atoms on the ablation resistance of ZBS systems in dynamic environments. The aim of the work would be to produce an UHTC that possess a tailorable emittance, exhibits strong thermal shock resistance, and improved ablation resistance. Thus, for this study, ZBS billets co-doped with Sm and Er atoms in five different ratios were prepared, with the nominal total dopant concentration constant at 3 mol% as showed in the Tan et al⁹ study. These samples were evaluated via ablation testing for 60 and 300 seconds using an oxyacetylene torch to evaluate how the Sm and Er dopants affect the oxidation process, and the final oxide phase(s) stability.

2 | EXPERIMENTAL PROCEDURE

2.1 | Materials and powder preparation

Spray-dried powders were prepared using the same method employed by Tan et al^{4,9} and the Brenner et al¹⁴ studies. Briefly, a laboratory spray dryer (APV Anhydro Model S1, Anhydro Inc, Soeborg, Denmark) was used to produce powder agglomerate from a liquid suspension feed (Aero-Instant Spraying Service, Brunswick, USA) that consisted of 80 vol% ZrB_2 (3–5 μm , Grade A, HC Starck, Munich, Germany), 20 vol% α -SiC (1.4 μm , Grade UF-05, HC Starck, Munich, Germany), 0.4 wt% dispersant (Darvan 821A, RT Vanderbilt Company, Inc, Norwalk, USA), 2 wt% PVA binder (Celvol 203, Celanese Corporation, Dallas, USA), and deionized

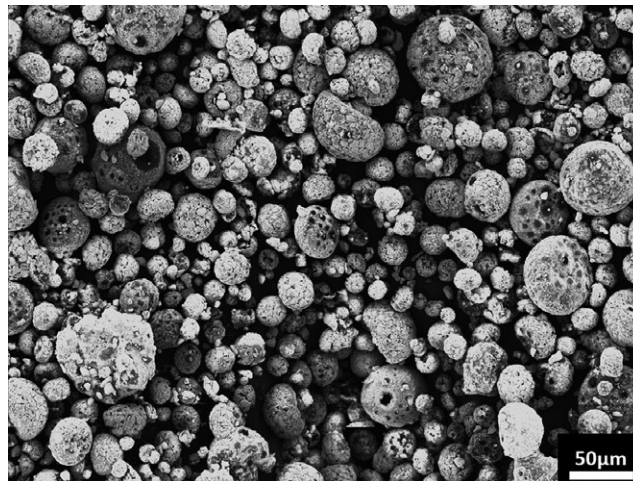


FIGURE 1 SEM electron micrographs of undoped spray-dried ZrB_2 -20 vol% SiC particles

water. The suspension was fed into the drying chamber by using a spraying nozzle, where the air was heated to 200°C. Next, a rotary atomizer spun at ~30 000 rpm was used to atomize the suspension into controlled-size droplets. The temperature at the outlet was ~105°C. The average particle size of the spray-dried particles, which was obtained by using a Malvern Mastersizer 2000 (Malvern Instrument Ltd., Worcestershire, UK), was approximately 38 μm . Figure 1 shows a SEM micrograph of the undoped spray-dried ZrB_2 -20 vol% SiC particles.

Samarium and/or erbium dopants were added to the spray-dried ZrB_2/SiC powders via a chemical infiltration method. In this process, samarium nitrate hexahydrate (99.9% pure $Sm(NO_3)_3 \cdot 6H_2O$, MSE Supplies, Arizona, USA) and/or erbium nitrate hexahydrate (99.9% pure $Er(NO_3)_3 \cdot 6H_2O$, MSE Supplies, Arizona, USA) were dissolved into 99.9% pure isopropyl alcohol, and the resulting solution was then infiltrated into the porous spray-dried ZrB_2/SiC powder. Solutions mixed in five different molar ratios (1Sm:0Er, 2Sm:1Er, 1Sm:1Er, 1Sm:2Er, and 0Sm:1Er) were prepared; the total rare-earth nitrate hexahydrate compound was added at an initial concentration of 10 mol%. Next, the alcohol and much of the water were removed via a rotary evaporator (BM 200, Yamato Scientific America Inc, Santa Clara, USA) at 100°C. This powder was heated at 500°C in air for an hour to remove residual water organics and nitrates. Tan et al⁴ performed a study of the normalized weight gain as a function of temperature from 200–1300°C demonstrating that below 600°C both the ZBS and the Sm-doped powders ZBS exhibited no weight gain that would be associated with oxidation. As the normalized weight gain was ~0 below 600°C, it suggests that the oxygen content does not increase during the heat treatment at 500°C. These results are consistent with temperature transitions reported by Bartuli et al¹⁵ for ZrB_2/SiC coatings, providing further evidence that the ZBS and the Sm-doped powders did not have any weight gain below

TABLE 1 Samarium and erbium dopant concentration and properties after sintering

	Sm(NO ₃) ₃ ·6H ₂ O Added (mol%)	Er(NO ₃) ₃ ·6H ₂ O Added (mol%)	Actual Sm Incorporated (mol%)	Actual Er Incorporated (mol%)	Bulk Density (g/cm ³)	Theoretical Density (g/cm ³)	Total Porosity (%)	Surface Roughness, Ra (nm)
1Sm:0Er	10	0	2.94	0	3.91	5.67	31.0	102 ± 12
2Sm:1Er	6.6	3.3	1.85	1.23	4.74	5.83	18.7	95 ± 15
1Sm:1Er	5	5	0.97	1.80	4.77	5.86	18.0	105 ± 14
1Sm:2Er	3.3	6.7	0.95	2.33	4.82	6.00	19.7	108 ± 8
0Sm:1Er	0	10	0	3.11	4.97	6.02	17.4	104 ± 11

All sintered billets nominally contained ZrB₂-20 vol% SiC. The bulk density calculation is based on final density after the sintering process.

600°C. The first weight gain inflections start near 600°C due to the oxidation of ZrB₂ to form *m*-ZrO₂ and B₂O₃ glass.⁴ After removal of organics, nitrates, and water at 500°C, the dried mixture was sieved using a 60-mesh (250 μm aperture) to eliminate large agglomerates. For ZBS powders/dopant ratios, ~20% by weight was lost during the 500°C heat treatment. These losses are due to the evaporation of the nitrates and water. ZBS powders with different ratios of Sm and/or Er dopants were die pressed at 82 MPa. The pressed billets were heated to 1650°C, held for 1 hour, heated to 2000°C, held for 15 minutes, and then cooled to room temperature. Sintering occurred in an argon atmosphere with graphite heating elements at a partial oxygen pressure of 10⁻⁷ ppm. Samples were cut into 25.4 mm × 25.4 mm squares.

Samples were final polished to ~0.1 μm using an auto polisher, where the samples were polished first to 6 μm and then to 3 μm. The bulk density of each billet for each ratio of Sm:Er was measured by the Archimedes methodology as described in the ASTM C373-88 standard. Surface roughness (R_a) was measured using an AFM (AS0200 AlphaStep, Tencor Corporation, Milpitas). To help simplify discussion, the naming convention uses the intended molar ratios. For instance, the 2Sm:1Er billet was to contain 6.66 mol% Sm(NO₃)₃·6H₂O and 3.33 mol% Er(NO₃)₃·6H₂O in the ZrB₂/SiC matrix. The actual amount of Sm and Er incorporated into the samples was measured by ICPMS with fusion preparation on pulverized billets (NSL Analytical Services Inc, Cleveland, USA).

2.2 | Oxyacetylene ablation testing

Heat flux conditions and ablation resistance were assessed using an oxyacetylene ablative torch rig. The test rig was constructed using ASTM E285-082 as a standard.¹⁶ The ablation torch (Victor Technologies, St. Louis) used a 5-mm orifice and a separation distance of 20 mm between the sample and the torch tip was held constant. An oxygen-rich environment was simulated using an oxygen:acetylene ratio of 12:10 slpm. The heat flux was measured to be 452 ± 6.8 W/cm² using a thermogage circular foil heat flux gauge (TG1000-4, Vatel Corp., Christiansburg, VA). The circular foil heat flux gauge has a water-cooler system which continuously provides an active heat sink that removes the absorbed heat, especially for applications with longer measurement times or high heat flux levels. Also, the thermogage sensor is coated with colloidal graphite. Front surface temperatures as a function of time were measured using a single-color pyrometer (OS3750, Omega Engineering Inc, Stamford, CT, USA) which was connected to a data logger. The single-color pyrometer has a target size for temperature measurements of 20 mm diameter which was positioned on the center of the sample where the flame was the hottest. The maximum temperature values from the target size area were measured at a spectral band

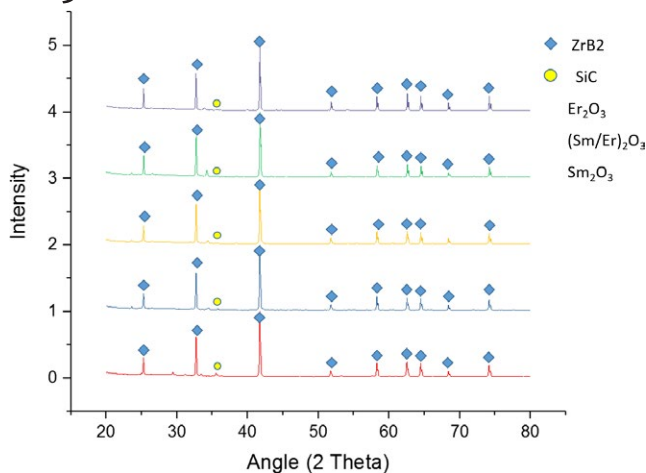


FIGURE 2 X-ray diffraction patterns of the surface of the preablated sintered samples

of 1.55 μm and reported with an accuracy rating of $\pm 1.2\%$ from the measured value. The emittance setting for the pyrometer was set to be 0.9. Five test specimens were exposed for 60 seconds and other five test specimens for 300 seconds. Samples were allowed to air cool to room temperature.

2.3 | Microstructural and phase analysis

Before performing the microstructural analysis, the samples were coated with a thin layer of Au/Pd. A scanning electron microscope (SEM) (Phillips XL-40, FEI Co., Hillsboro, USA) was used to characterize billet topography in the preablated and post-ablated conditions. X-ray diffraction (XRD) (D8 Focus, Bruker Corporation, Billerica, USA) was used to identify the phases present using $\text{CuK}\alpha$ radiation for 2θ values of 20° – 80° on the billets before ablation, and for 2θ values of 15° – 80° after ablation. A step size of 0.02° and a scan rate of $5^\circ/\text{min}$ were used for all samples. Samples were positioned in the XRD to analyze the regions where the ablation flame was most intense.

3 | RESULTS

3.1 | Preablated sintered samples results

The actual concentrations of Sm (mol%) and Er (mol%) incorporated into each billet are listed in Table 1, along with the measured bulk density, theoretical density, total porosity (%), and surface roughness. It was observed that ~ 3 mol% rare-earth element(s) were incorporated into the sintered billets, $\sim 1/3$ of the 10 mol% rare-earth nitrate hexahydrate compounds during the chemical doping process. It should be noted that most of this reduction in the dopant concentration was caused by the heat treatment at 500°C where the water, organics, and nitrates were removed, and not because

the Sm and Er were lost. Recall that the 10 mol% added during the chemical doping process is referring to the combined $\text{Sm}(\text{NO}_3)_3 \cdot 6\text{H}_2\text{O}$ and $\text{Er}(\text{NO}_3)_3 \cdot 6\text{H}_2\text{O}$. Therefore, the combined concentrations of Sm (mol%) and Er (mol%) represents $\sim 35\%$ (~ 3.5 mol%) of 10 mol% added during the chemical doping process. As ~ 3 mol% dopant(s) were incorporated into the sintered billets, it can be concluded that the remainder ~ 0.5 mol% was lost during powder handling or during sintering. These results are different than the ones presented in Tan et al^{4,9} studies and Brenner et al¹⁷ study where 5 mol% Sm dopant was incorporated into plasma-sprayed coatings. The decrease of the ~ 2 mol% of the dopant(s) incorporated into the sintered billets of the present study were caused by the different method used to prepare the samples, as the samples used in Tan et al^{4,9} studies and Brenner et al¹⁷ study were prepared using a plasma spray process.

Table 1 shows more Er dopant was integrated into the sample than the Sm dopant. This is apparent by comparing the 1Sm:0Er and 0Sm:1Er billets, where 2.94 mol% of Sm and 3.11 mol% of Er were incorporated, respectively. This difference is explained by the differences in their molar mass, where Sm represents the 33.8% of the 10 mol% $\text{Sm}(\text{NO}_3)_3 \cdot 6\text{H}_2\text{O}$ added during the chemical doping process for the 1Sm:0Er billet, whereas Er represents 36.3% of the 10 mol% $\text{Er}(\text{NO}_3)_3 \cdot 6\text{H}_2\text{O}$ added for the 0Sm:1Er billet. Surface roughness ($R_a \sim 100$ nm) were all similar, consistent with using the same polishing procedures for each billet investigated. Samples ranged in total porosity from 17% to 31%.

X-ray diffraction results on the billets before ablation testing presented in Figure 2 indicated ZrB_2 is the majority phase with a small peak at 35.5° identified as α -SiC. For the 1Sm:0Er and 0Sm:1Er samples, the small intensity peaks between 2θ of 23° – 35.5° correspond to Sm_2O_3 and Er_2O_3 , respectively. For the 2Sm:1Er, 1Sm:1Er, and 1Sm:2Er preablated samples, the XRD results shows a similar $(\text{Sm}/\text{Er})_2\text{O}_3$ phase due to the Sm and Er atoms exchanging positions because of their similar ionic size (242 pm for Sm and 236 pm for Er). The peaks were shifted to larger 2θ due to the smaller interplanar spacing caused by the slightly smaller erbium atoms. As noted in the XRD results, the Sm and Er compounds and alloys oxidized to some extent in the high purity Ar atmosphere during the sintering process.

Figure 3A-E compares the SEM micrographs of the surface of the billets before the ablation testing. The XRD results in Figure 2 indicating the primary phase to be ZrB_2 were further verified by EDS results for each sample which showed ZrB_2 grains of approximately a 1:2 ratio of Zr to B atoms. The grains were surrounded by a matrix composed of mainly Sm and Er with small portions of O, Si, and C. The small portion of Si and C in the EDS results also matches with the small α -SiC peak identified at 35.5° in the XRD plot in Figure 2.

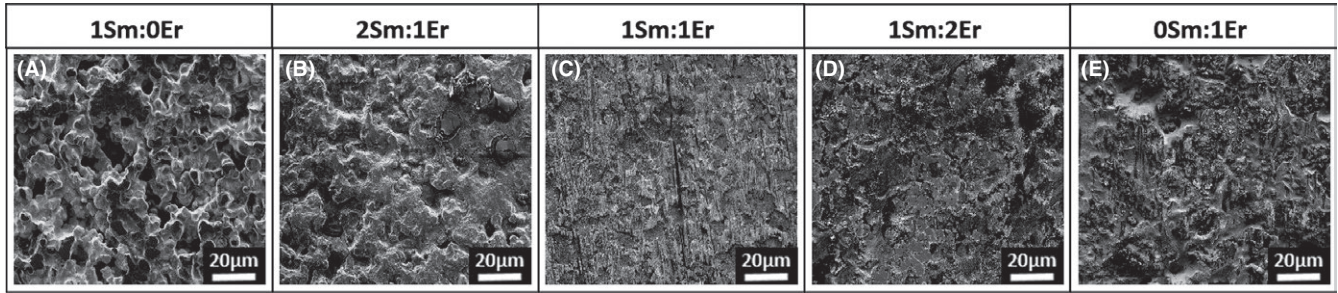


FIGURE 3 SEM electron micrographs of the surface of the preablated-sintered samples for: (A) 1Sm:0Er, (B) 2Sm:1Er, (C) 1Sm:1Er, (D) 1Sm:2Er, and (E) 0Sm:1Er

3.2 | Ablation results after 60 seconds

Figure 4A shows a plot of front surface temperature as a function of time during the 60 seconds ablation cycle for each of the five billets tested. All the samples displayed a continuous temperature increase through the 60 seconds of heating, with a rapid increase in temperature followed by a much slower increase in temperature. The maximum temperatures during the ablation cycle were the highest for the 0Sm:1Er and 1Sm:2Er samples at $1717 \pm 21^\circ\text{C}$ and $1715 \pm 21^\circ\text{C}$, respectively, and the lowest for the 2Sm:1Er sample at $1612 \pm 19^\circ\text{C}$. The maximum temperatures for the 1Sm:0Er and 1Sm:1Er samples were $1690 \pm 20^\circ\text{C}$ and $1672 \pm 20^\circ\text{C}$, respectively. The temperature at which the rate of heating slows down is different for all the samples. The inflection point temperature was the highest for the 0Sm:1Er sample at $1600 \pm 19^\circ\text{C}$ after ablating for 12 seconds, and the lowest for the 2Sm:1Er sample $1300 \pm 16^\circ\text{C}$ after ablating for 9 seconds.

Figure 5A-E compares the ablated surfaces after the 60 seconds ablation cycle. Each of the Sm:Er billets developed an adherent oxide scale. The oxide scale color changes relative to the amount of Sm and Er dopant from yellow in the 1Sm:0Er sample to pink in the 0Sm:1Er sample.

Figure 6A-E compares SEM micrographs of the surface of the billets after ablating for 60 seconds. For all the Sm:Er samples, the surface appears to have clusters of faceted islands surrounded by an bulbous phase. Figure 6A-C shows that the faceted islands become larger as the Sm concentration is increased from 0.97 mol% in the 1Sm:1Er sample to 2.94 mol%

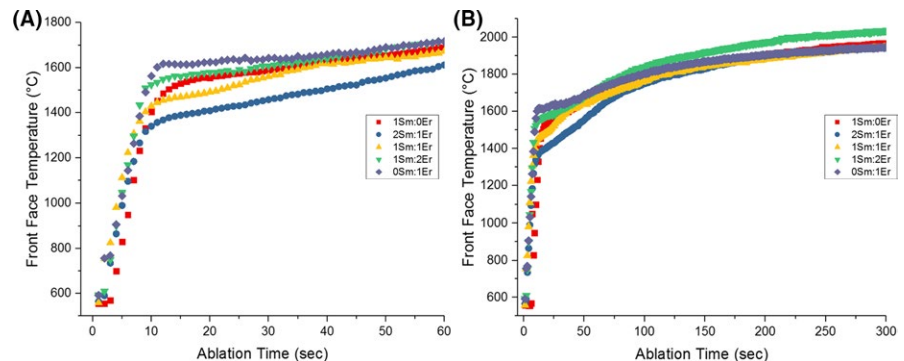
in the 1Sm:0Er sample. Additionally, the 1Sm:1Er billet shows the presence of pores and dendrites, while the 1Sm:0Er billet shows a “flower-like” microstructure.

The post-ablation XRD results for the 1Sm:0Er sample presented in Figure 7A match with previous studies,⁹ where the major phase formed was the cubic samarium zirconium oxide scale ($c_1\text{-Sm}_{0.2}\text{Zr}_{0.8}\text{O}_{1.9}$, JCPDS-01-78-1302). For the ablated 2Sm:1Er, 1Sm:1Er, and 1Sm:2Er billets samples, the XRD results shows a similar cubic structure ($c_1\text{-(Sm/Er)}_{0.2}\text{Zr}_{0.8}\text{O}_{1.9}$) as the major phase due to the Sm and Er atoms exchanging positions because of their similar ionic size (242 pm for Sm and 236 pm for Er). The primary peaks were shifted to larger 2θ due to the smaller interplanar spacing caused by the slightly smaller erbium atoms. Lattice parameters of 0.517, 0.513, 0.511, 0.510, and 0.507 nm were measured for $c_1\text{-(Sm/Er)}_{0.2}\text{Zr}_{0.8}\text{O}_{1.9}$ for the 1Sm:0Er, 2Sm:1Er, 1Sm:1Er, 1Sm:2Er, and 0Sm:1Er samples, respectively. These results follow the Vegard's law as the interplanar spacing decrease almost linearly as the Sm dopant concentration is increased. Small portions of monoclinic zirconia ($m\text{-ZrO}_2$, JCPDS-00-37-1484) were also observed. Finally, the ablated 0Sm:1Er sample was primarily cubic erbium zirconium oxide scale ($c_1\text{-Er}_{0.2}\text{Zr}_{0.8}\text{O}_{1.9}$) with small amounts of $m\text{-ZrO}_2$.

3.3 | Ablation results after 300 seconds

The ablation results of the samples evaluated for 60 seconds were compared with the first 60 seconds of the

FIGURE 4 Front surface temperature during ablation testing for (A) 60 seconds and (B) 300 seconds



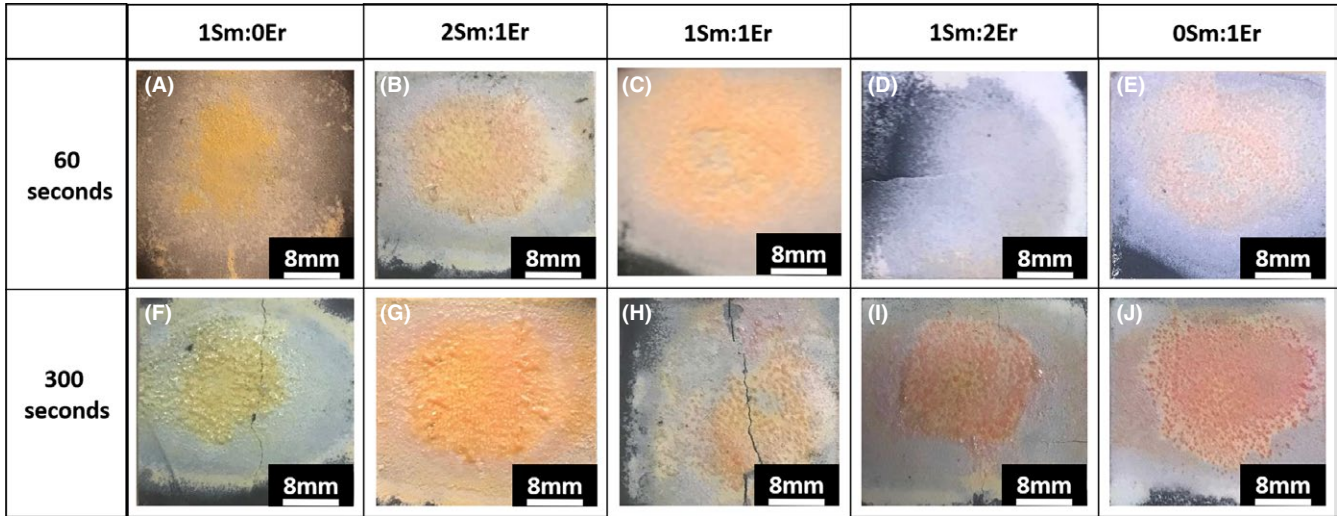


FIGURE 5 Optical images of the ablated billets: A, 1Sm:0Er, B, 2Sm:1Er, C, 1Sm:1Er, D, 1Sm:2Er, and E, 0Sm:1Er after 60 seconds, and F, 1Sm:0Er, G, 2Sm:1Er, H, 1Sm:1Er, I, 1Sm:2Er, and J, 0Sm:1Er after 300 seconds

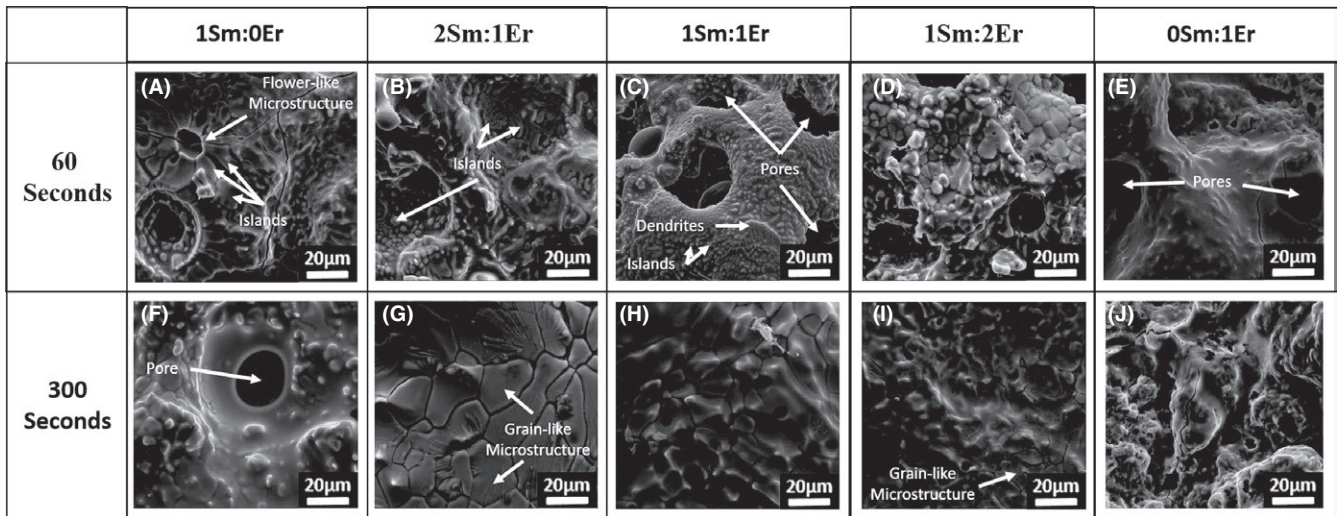


FIGURE 6 SEM electron micrographs of the following billets: A, 1Sm:0Er, B, 2Sm:1Er, C, 1Sm:1Er, D, 1Sm:2Er, and E, 0Sm:1Er after 60 seconds, and F, 1Sm:0Er, G, 2Sm:1Er, H, 1Sm:1Er, I, 1Sm:2Er, and J, 0Sm:1Er after 300 seconds

samples ablated for 300 seconds to test the variation of the temperature measurements with time. The standard deviation of each time point was calculated, and then, these 60 standard deviation values were used to calculate their 95% confidence interval. The variations of the temperature measurements were small, varying from $37 \pm 4.2^\circ\text{C}$, $8.8 \pm 4.3^\circ\text{C}$, $8.3 \pm 4.1^\circ\text{C}$, $5.9 \pm 3.2^\circ\text{C}$, and $8.1 \pm 4.2^\circ\text{C}$ for the compositions 1Sm:0Er, 2Sm:1Er, 1Sm:1Er, 1Sm:2Er, and 0Sm:1Er, respectively.

Figure 4B shows the front surface temperature during the 300 seconds ablation cycle. The maximum temperature during the ablation cycle was the highest for the 1Sm:2Er sample at $2037 \pm 24^\circ\text{C}$. The maximum temperatures of $1968 \pm 24^\circ\text{C}$, $1946 \pm 23^\circ\text{C}$, $1947 \pm 23^\circ\text{C}$, and $1947 \pm 23^\circ\text{C}$ were measured for the 1Sm:0Er, 2Sm:1Er, 1Sm:1Er, and

0Sm:1Er samples, respectively. During the first 100 seconds of ablation, the 2Sm:1Er sample showed the lowest front face temperature. Excluding the 1Sm:2Er sample, the temperature difference between the other four compositions studied after ablation for 100 seconds seem to be very similar. All the samples displayed a continuous temperature increase through the 300 seconds of heating but were significantly hotter ($\sim 300^\circ\text{C}$) than the samples ablated for 60 seconds. As the ablation time is increased from 60 to 300 seconds, a second inflection point, in addition to the first one previously described, can be seen for all the five Sm:Er molar ratios. The inflection point occurs at approximately $1700 \pm 20^\circ\text{C}$ after ablation for 75 seconds.

Figure 5F-J shows the ablation surface micrograph comparison of the samples after the 300 seconds ablation

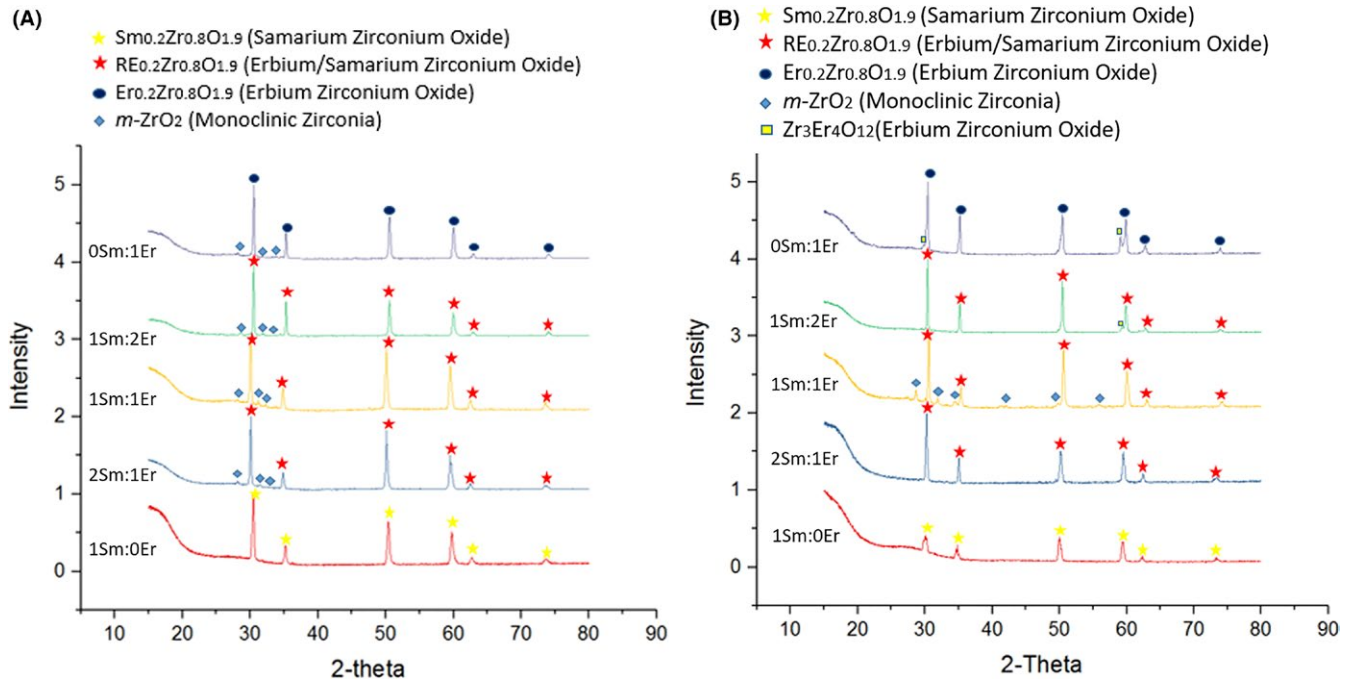


FIGURE 7 X-ray diffraction patterns of the surface after (A) 60 seconds and (B) 300 seconds ablation cycles

cycle. Each of the Sm:Er billets developed an adherent oxide scale. The oxide scale color changes relative to the amount of Sm and Er dopant as in the 60 seconds ablation cycle from yellow in 1Sm:0Er to pink in 0Sm:1Er. It was observed that more amorphous phase was present when the ablation time was increased from 60 to 300 seconds. It should be noted that the cracks shown on the 1Sm:0Er and 1Sm:1Er samples were caused by removing the samples from the ablation rig.

Figure 6F-J presents the surface topography of the ablated samples after 300 seconds. The faceted islands observed in the first 60 seconds of ablation for the 2Sm:1Er, 1Sm:1Er, and 1Sm:2Er samples, have increased in size and coalesced. Therefore, a grain-like structure is evident in the three samples containing both Sm and Er dopants (Figure 6G-I). A morphology consistent with an amorphous phase is covering portions of the grain-like structure in Figure 6I-J. The amount of glassy phase on these three samples appears to increase as the Er concentration increases. On the contrary, the 1Sm:0Er and 0Sm:1Er samples did not show the grain-like structure. Figure 6F shows that in the 1Sm:0Er sample the faceted islands formed after 60 seconds have increased in size but maintained an interpenetrating amorphous morphology surrounding them. Figure 6J shows that the 0Sm:1Er sample exhibits a similar microstructure as the 1Sm:0Er.

Figure 7B shows the XRD results obtained from the surface of the samples after the 300 seconds ablation cycle. The XRD of the samples after ablation for 300 seconds

remains unchanged, being primarily composed of $c1\text{-}(\text{Sm}/\text{Er})_{0.2}\text{Zr}_{0.8}\text{O}_{1.9}$ as the major phase with small amounts of $m\text{-ZrO}_2$ observed. More amorphous phase, as evidenced by the broadband signal increase below $20^\circ 2\theta$ in the Figure 7B XRD data, is apparent after 300 seconds of ablation.

A typical EDS line scan for a sample ablated for 300 seconds is shown in Figure 8. For the 2Sm:1Er sample shown, the Sm and Er dopant concentration is much higher at the ablated surface ($x = 0 \mu\text{m}$) than in deeper regions of the billet. The average Sm and Er concentration between $x = 0\text{-}75 \mu\text{m}$ (within the oxide scale), as shown in Figure 8, is $\sim 30 \text{ wt}\%$ for Sm and $\sim 20 \text{ wt}\%$ for Er. The $c1\text{-}\text{Sm}_{0.2}\text{Zr}_{0.8}\text{O}_{1.9}$ phase requires $\sim 23 \text{ wt}\%$ Sm to form, whereas the $c1\text{-}\text{Er}_{0.2}\text{Zr}_{0.8}\text{O}_{1.9}$ phase requires $\sim 20 \text{ wt}\%$ Er to form. As the distance from the ablated surface is further increased, the average combined Sm and Er concentration between $x = 75\text{-}250 \mu\text{m}$ as shown in Figure 8, is $\sim 16 \text{ wt}\%$. It is worth noting that the concentration difference between Sm and Er decreases as the distance from the ablated surface is increased. On the contrary, the Zr concentration is much lower at the ablated surface than in deeper regions of the billet. The average Zr concentration between $x = 0\text{-}75 \mu\text{m}$ (within the oxide scale), as shown in Figure 8, is $\sim 45 \text{ wt}\%$. As the distance from the ablated surface is further increased, the average Zr concentration between $x = 75\text{-}250 \mu\text{m}$ is $\sim 75 \text{ wt}\%$. Based on the Figure 8 EDS line scan, it can be concluded that as the distance from the ablated surface is increased, the amount of the $c1\text{-}(\text{Sm}/\text{Er})_{0.2}\text{Zr}_{0.8}\text{O}_{1.9}$ phase decreases, and the amount of the $m\text{-ZrO}_2$ phase increases.

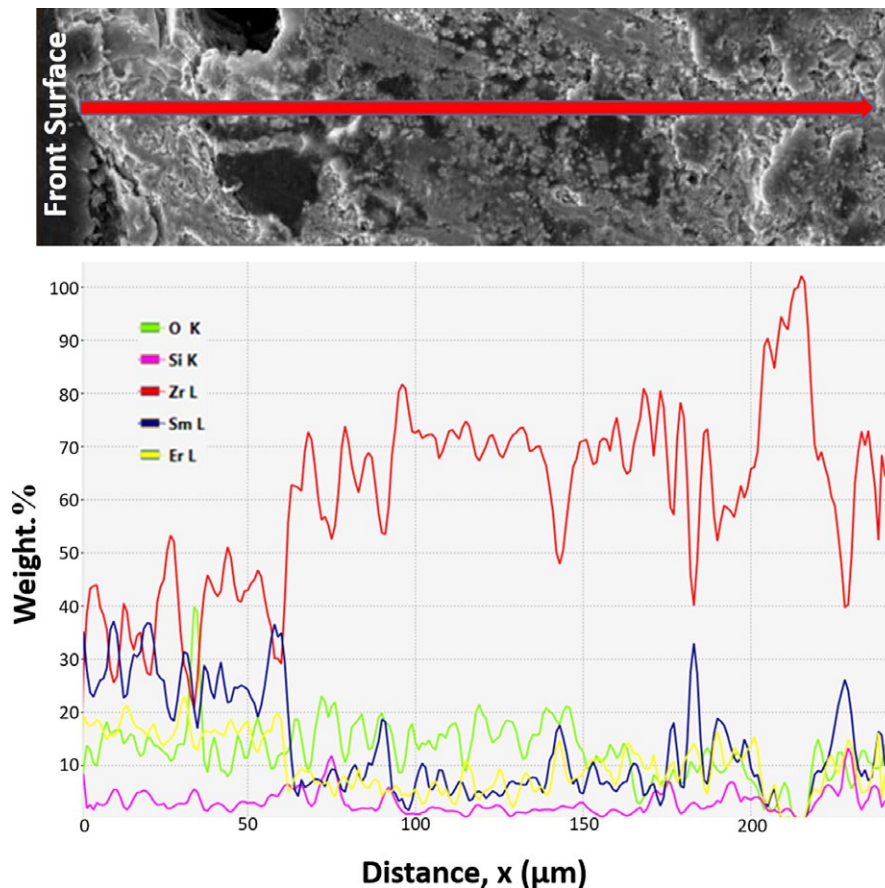


FIGURE 8 EDS line-scan for the 2Sm:1Er sample after 300 seconds ablation cycle and the wt% concentration of major elements across the ablated billet thickness

4 | DISCUSSION

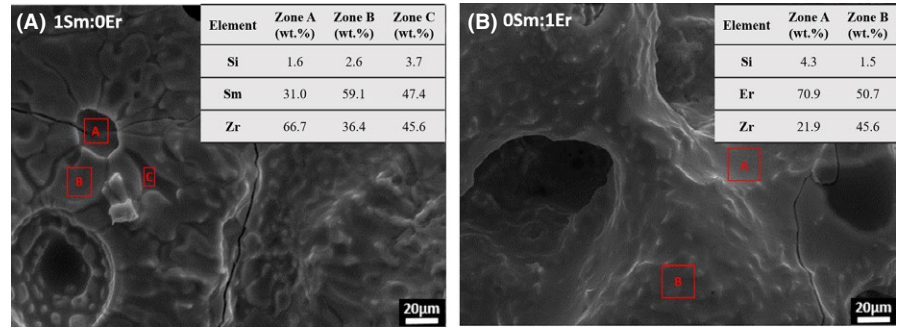
4.1 | First observation: The beneficial samarium/erbium zirconium oxide scale noted after ablation for 60 seconds and 300 seconds is formed by a convection cells mechanism

This study investigates the ablation properties of the oxide scales formed during ablation when emittance modifiers of Sm and Er are added. The crystalline and amorphous phases observed in Figure 6 are being formed by a convection cell mechanism. These convection cells were noted by Karlsdottir et al¹⁸ for ZrB₂/SiC coatings during oxidation at 1550°C as a flower-like microstructure. The study described the “islands” (center regions of the flower-like structure) to be *m*-ZrO₂, the “petals” to be B₂O₃ glass, and the “lagoon” regions to be SiO₂ glass.¹⁸ The formation of the flower-like structure is caused by the viscous fingering phenomenon, which is the displacement of a less viscous liquid.^{18,19} Due to the instability of the moving interface, the less viscous B₂O₃ liquid displaces a more viscous SiO₂ liquid.^{18–20} The rising B₂O₃-rich liquid contains dissolved ZrO₂, which deposits in the center of the flower-like structure when the B₂O₃ evaporates. The liquid

boria-rich oxidation product is transported through the overlying layer of SiO₂ liquid by convection, forming convection cells aligned like the petals of a flower.^{14,18–20}

Brenner et al¹⁷ also noted these convection cells during the oxidation of Sm-doped ZrB₂/SiC coatings at ~1700°C. Even though the convection cells mechanism during the ablation process in the present study was very similar compared to both Brenner et al¹⁷ and Karlsdottir et al^{18,19} studies, the final ablation product is different. The addition of Sm dopant to the ZrB₂/SiC coatings in Brenner et al¹⁷ study formed a Sm-stabilized *t*-ZrO₂ phase after ablation, whereas the Karlsdottir et al^{18,19} studies final product was *m*-ZrO₂. Studies have shown that the B₂O₃ glass present on the surface of a Sm-doped ZrB₂/SiC coating after heating to 900°C contains Sm³⁺ atoms.⁹ It is expected that the B₂O₃ glass formed in the present study would not only contain Sm³⁺ atoms but also Er³⁺ atoms. This was confirmed by the SEM-EDS image shown in the Figure 9A, where 31.0, 59.1, and 47.4 wt% of Sm were detected in zones A-C, respectively; while 71.0 and 51.0 wt% of Er were detected in zones A-B in the Figure 9B. Because of the Sm³⁺ and Er³⁺ atoms being present in the rising B₂O₃-rich liquid containing dissolved ZrO₂, the final oxide scale product formed during the ablation testing will be

FIGURE 9 SEM-EDS for: A, micrograph of the flower-like microstructure on the 1Sm:0Er billet after the 60 seconds ablation cycle; B, micrograph of the 0Sm:1Er billet after the 60 seconds ablation cycle



different. This was confirmed by the XRD results on Figure 7A-B and the SEM-EDS of Figure 9A where the center region of the “flower-like” structure is composed of the crystalline c_I - $\text{Sm}_{0.2}\text{Zr}_{0.8}\text{O}_{1.9}$, instead of the m - ZrO_2 reported in the Karlsdottir et al^{18,19} studies or the Sm-stabilized t - ZrO_2 phase in Brenner et al¹⁷ study.

The evaporation of B_2O_3 glass would be expected as the maximum front surface temperatures were $1690 \pm 20^\circ\text{C}$ and $1717 \pm 21^\circ\text{C}$ during the 60 seconds ablation tests for the 1Sm:0Er and 0Sm:1Er billets, respectively. Based on these surface temperatures it is also expected that much of the SiO_2 glass would be evaporated, consistent with the small amounts of Si detected in the EDS results presented in Figure 9A-B.

Even though the powder preparation and the ablation test parameters used in the present study were the same than the ones used in the Brenner et al¹⁷ study, the resulted final oxide scale was different. This difference occurred because the alumina substrates in the Brenner et al¹⁷ study became part of the system by forming a blister after the ablation for 60 seconds due to a local eutectic reaction occurring between Sm_2O_3 , ZrO_2 , and Al_2O_3 , and therefore, inhibited the formation of the c_I - $\text{Sm}_{0.2}\text{Zr}_{0.8}\text{O}_{1.9}$ reported for the 1Sm:0Er sample in the present study. If the problem of the alumina substrate becoming part of the system in the Brenner et al¹⁷ study is avoided, the c_I - $\text{Sm}_{0.2}\text{Zr}_{0.8}\text{O}_{1.9}$ oxide phase will be formed, consistent with Tan et al^{4,9} studies and the present study.

The only difference in the XRD results between the samples ablated for 60 seconds and 300 seconds is the evidence of more glassy phase after longer ablation times, as observed by larger amorphous humps at lower values of 2θ for each of the Sm:Er billets investigated. The glassy phase seems to be more evident as Er concentration increased. The increase in the amount of the glassy phase makes sense with the assertions in previous studies,^{9,19,21} where the addition of rare-earth element dopants to ZrB_2/SiC billets modifies the tetrahedron structure of B_2O_3 and SiO_2 resulting in the reduction of the viscosity of the glass and melting temperature. As the theoretical density of samarium oxide (7.62 g/cm^3) is lower than erbium oxide (8.64 g/cm^3), the viscosity should be reduced even more as the Sm concentration increases. This relationship between reduction of viscosity and increase of glassy phase is evident for the ablated billets after 300 seconds of

this study. The increased glassy phase formed as the ablation time is increased from 60 to 300 seconds is preventing conduction of heat away from the surface resulting in an increase of the front surface temperature. Therefore, it is expected that this glassy phase might affect the emittance, but future studies need to be performed to confirm this assertion.

With increased time at high temperature, the glassy phase submerges the convection cells and they essentially disappear. Even though we cannot see the convection cells in the final microstructure after ablation, their effect on the final microstructure can be noted by the presence of c_I -(Sm/Er) $_{0.2}\text{Zr}_{0.8}\text{O}_{1.9}$ crystalline islands surrounded by a glassy phase. Occasionally remnants of the convection cells can be observed in the final microstructure. For example, a “flower-like” structure is noted in Figure 6A for the 1Sm:0Er sample. After ablation for 300 seconds, the c_I -(Sm/Er) $_{0.2}\text{Zr}_{0.8}\text{O}_{1.9}$ islands grow, coalesce, and inhibit the formation of petals by forming the crystalline grains shown in Figure 6G, H, and I.^{19,22}

Overall, the convection cell mechanism occurring in the present study is similar to both Karlsdottir et al^{18,19} and Brenner et al¹⁷ studies. However, significant differences are shown due to the rare-earth element dopants used in the present study which cause the formation of different oxide scales during ablation testing. As the main purpose of doping the ZBS systems with emittance modifiers as Sm and Er is to form a c_I -(Sm/Er) $_{0.2}\text{Zr}_{0.8}\text{O}_{1.9}$ phase, the Sm-stabilized t - ZrO_2 in the Brenner et al¹⁷ study and the m - ZrO_2 in the Karlsdottir et al^{18,19} studies do not offer any improvement in modifying the emittance and the Sm^{3+} ions role in the final microstructure is limited. The ability to increase the emissivity by forming the c_I - $\text{Sm}_{0.2}\text{Zr}_{0.8}\text{O}_{1.9}$ instead of m - ZrO_2 was confirmed by Tan et al⁹ study by increasing the emissivity up to 0.9 at 1600°C for a coating constituted of 5 mol% Sm with a balance of ZrB_2/SiC . Therefore, it can be concluded that a similar c_I -(Sm/Er) $_{0.2}\text{Zr}_{0.8}\text{O}_{1.9}$ with different Sm:Er ratios will produce differences in the spectral emittance. As a result, the c_I -(Sm/Er) $_{0.2}\text{Zr}_{0.8}\text{O}_{1.9}$ is a more desirable oxide product because it produces a potential tailorable spectral emittance oxide scale; whereas forming a more stable and ablation resistance oxide scale than both the m - ZrO_2 formed on Karlsdottir et al^{18,19} studies, and the Sm-stabilized t - ZrO_2 on

Brenner et al.¹⁷ study. Furthermore, the c_1 -Sm_{0.2}Zr_{0.8}O_{1.9} has a melting point of 2700°C for 3 mol% of Sm dopant which is similar to the one of m -ZrO₂.⁹

Finally, the fact that the beneficial c_1 -(Sm/Er)_{0.2}Zr_{0.8}O_{1.9} provides a more dense oxide scale than m -ZrO₂ typically formed on ZBS systems, could help to address the one of the most damaging factors to ZBS systems caused by the porous m -ZrO₂ scale that does not provide any barrier to oxygen transport and tends to detach from the base alloy. Hence, the beneficial c_1 -(Sm/Er)_{0.2}Zr_{0.8}O_{1.9} oxide scale formed in the surface, will reduce the amount of oxygen transported to deeper parts of the billet where the concentration of m -ZrO₂ is higher as showed by the EDS line-scan on Figure 8. This fact was also reported by Tan et al.⁹ who showed that the c_1 -Sm_{0.2}Zr_{0.8}O_{1.9} oxide scale formed for ZBS coatings doped with 3 mol% of Sm is denser than m -ZrO₂ formed for ZBS coatings.

4.2 | Second observation: Changes in the surface Sm and Er dopant concentration affects surface temperature measured

Despite the similarities of the convection cell mechanism in the billets prepared with five different Sm:Er molar ratios, the heating rates vary as can be noted by the difference in the inflection points observed in Figure 3A-B. For example, Figure 4A shows that the inflection point temperature was the highest for the 0Sm:1Er sample at $1600 \pm 19^\circ\text{C}$ after ablation for 12 seconds, and the lowest for the 2Sm:1Er sample $1300 \pm 16^\circ\text{C}$ after ablation for 9 seconds. These differences in the inflection points can be explained by the different compositions of Sm³⁺ and Er³⁺ atoms in the billets which change the emittance and the spectral absorbance of the oxide scales formed during ablation.

Changes in the emittance caused by using Sm³⁺ dopant have been shown in previous studies which demonstrated that the emittance of ZrO₂ can be increased via doping with rare-earth oxides which intentionally introduce defects into a pure material.^{9,23} By comparing the ionic conductivity of the c_1 -(Sm/Er)_{0.2}Zr_{0.8}O_{1.9} phase formed in the present study with the m -ZrO₂, it is important to note that the ionic conductivity will increase for the c_1 -(Sm/Er)_{0.2}Zr_{0.8}O_{1.9}, as the incorporated Sm³⁺ and Er³⁺ ions creates oxygen vacancies.^{9,22} These oxygen vacancies provide transitions within the material band gap which modify the emittance.^{9,22} Figure 8 shows that the amount of m -ZrO₂ increases as the distance from the ablated surface is further increased. Based on that, the ionic conductivity should be higher in the ablated surface than in deeper regions of the billets.

Samarium oxide has demonstrated high emittance from visible to near IR wavelengths.¹² It is expected that the emittance will generally increase as the Sm³⁺ concentration is raised. Hence, increases in the heating rate may result from changes in emittance upon heating of such rare-earth element doped coatings. Previous evaluation of Sm-doped ZrB₂/SiC

coatings demonstrate that the Sm³⁺ atoms concentration is much higher at the ablated surface in comparison with Sm³⁺ atoms concentration in the bulk.⁹ Figure 8 shows the rare-earth element dopant concentration is much higher in the ablated surface than in the bulk. Therefore, it is expected that the concentration dependent emittance in the 2Sm:1Er billet will be higher than in the 1Sm:2Er sample. Thus, ultimate temperature observed is lower for Sm-rich coatings and considerable inflection points in temperature are observed for Sm-rich coatings in Figure 4B.

On the other hand, it is well known that erbium oxide has demonstrated a low emittance in several wavelength ranges.¹² As the emittance for the current work was set to 0.9 on the pyrometer, the temperature would be underestimated if the emittance of the oxidized surface is lower at 1.55 μm. Alternatively, if the surface is reradiating less efficiently for a given temperature or becoming more absorptive at torch wavelengths, such coatings would heat more rapidly and/or achieve a higher ultimate temperature. After ablation for 60 seconds, it is shown that as the Er³⁺ concentration is increased and the resulting c_1 -(Sm/Er)_{0.2}Zr_{0.8}O_{1.9} oxide scale is either more absorptive at torch wavelengths and/or reradiating less efficiently, and therefore, achieving a higher surface temperature for Er-rich billets. In Figure 4A, the maximum temperatures during the ablation cycle were the highest for the 0Sm:1Er and 1Sm:2Er samples; and the lowest for the 2Sm:1Er sample. However, this relation cannot be fully established as the ablation time is further increased from 60 to 300 seconds. Figure 4B shows that maximum temperatures during the ablation cycle was the highest for the 1Sm:2Er sample, and lower for the 1Sm:0Er, 2Sm:1Er, 1Sm:1Er, and 0Sm:1Er samples. As can be noted by the results after ablation for 300 seconds, the maximum temperatures of the 1Sm:0Er, 2Sm:1Er, 1Sm:1Er, and 0Sm:1Er samples were very similar, and therefore, the benefit of being able to control the emittance and absorption properties by varying the Sm³⁺ and Er³⁺ concentration is not clear. As the only difference in the XRD results after ablation for 60s and 300s in Figure 7A-B is the evidence of more glassy phase after longer ablation times, as observed by larger amorphous humps at lower values of 2θ, it is evident that the increase in glassy phase is inhibiting the beneficial effects of increasing the emittance as the Sm³⁺ concentration is increased from 0-2.94 mol%. A possible solution to avoid this problem and maximize the beneficial effects of tailoring the emittance at these higher temperatures shown by Figure 4B is to increase the total dopant(s) concentration incorporated into the sample from 3 mol% to 5 mol% as in Tan et al.⁹ study.

5 | CONCLUSIONS

Sintered ZrB₂/SiC billets co-doped with Sm and Er atoms in five different ratios were prepared. These samples were

evaluated via ablation testing for 60 and 300 seconds using an oxyacetylene torch. The phase assemblage and microstructure of the surface were evaluated after each ablation time. ZBS billets co-doped with Sm and Er forms a potential tailorable emittance $c_f\text{-(Sm/Er)}_{0.2}\text{Zr}_{0.8}\text{O}_{1.9}$ oxide scale as the major phase, which provides a more stable oxide scale than the $m\text{-ZrO}_2$ oxide scale formed in ZBS systems. The crystalline oxide scale and amorphous phases form by a convection cells mechanism where the $c_f\text{-(Sm/Er)}_{0.2}\text{Zr}_{0.8}\text{O}_{1.9}$ crystalline islands precipitate, grow and coalesce. Changes in the surface Sm and Er dopant concentration affects surface temperature measured due to changes in spectral emittance upon heating.

ACKNOWLEDGMENTS

The authors acknowledge the financial support of Dr. Ali Sayir of the Air Force Office of Scientific Research (AFOSR Grant # FA9550-16-1-0039). The authors also acknowledge Anneliese E. Brenner for providing the SEM electron micrograph of the undoped spray-dried ZrB₂-20 vol% SiC particles showed in the Figure 2.

ORCID

Angel A. Peña  <https://orcid.org/0000-0002-5827-0893>

REFERENCES

1. Squire T, Marschall J. Material property requirements for analysis and design of UHTC components in hypersonic applications. *J Eur Ceram Soc.* 2010;30(11):2239-51.
2. Mack A. Aerothermodynamic behaviour of a generic nose cap model including thermomechanical structural effects. *Aerospace Sci Technol.* 2007;11(5):386-95.
3. Tan W, Adducci M, Trice R. Evaluation of rare-earth modified ZrB₂-SiC ablation resistance using an oxyacetylene torch. *J Am Ceram Soc.* 2014;97(8):2639-45.
4. Tan W, Petorak C, Trice R. Rare-earth modified zirconium diboride high emissivity coatings for hypersonic applications. *J Eur Ceram Soc.* 2014;34(1):1-11.
5. Monteverde F. The thermal stability in air of hot-pressed diboride matrix composites for uses at ultra-high temperatures. *Corros Sci.* 2005;47(8):2020-33.
6. Monteverde F, Savino R. Stability of ultra-high-temperature ZrB₂-SiC ceramics under simulated atmospheric re-entry conditions. *J Eur Ceram Soc.* 2007;27(16):4797-805.343.
7. Tului M, Marino G, Valente T. Plasma spray deposition of ultra high temperature ceramics. *Surf Coat Technol.* 2006;201(5):2103-8.
8. Li H, Zhang L, Cheng L, Wang Y. Ablation resistance of different coating structures for C/ZrB₂-SiC composites under oxyacetylene torch flame. *Int J Appl Ceram Technol.* 2009;6(2):145-50.
9. Tan W, Adducci M, Petorak C, Thompson B, Brenner A, Trice R. Effect of rare-earth dopant (Sm) concentration on total hemispherical emissivity and ablation resistance of ZrB₂/SiC coatings. *J Eur Ceram Soc.* 2016;36(16):3833-41.
10. Ilic O, Bermel P, Chen G, Joannopoulos J, Celanovic I, Soljačić M. Tailoring high-temperature radiation and the resurrection of the incandescent source. *Nat Nanotechnol.* 2016;11(4):320-4.
11. Lin S, Moreno J, Fleming J. Three-dimensional photonic-crystal emitter for thermal photovoltaic power generation. *Appl Phys Lett.* 2003;83(2):380-2.
12. Lenert A, Bierman DM, Nam Y, Chan WR, Celanović I, Soljačić M, et al. A nanophotonic solar thermophotovoltaic device. *Nat Nanotechnol.* 2014;9(2):126-30.
13. Guazzoni G. High-temperature spectral emittance of oxides of Erbium, Samarium, Neodymium and Ytterbium. *Appl Spectrosc.* 1972;26(1):60-5.
14. Padovano E, Badini C, Celasco E, Biamino S, Pavese M, Fino P. Oxidation behavior of ZrB₂/SiC laminates: Effect of composition on microstructure and mechanical strength. *J Eur Ceram Soc.* 2015;35(6):1699-714.
15. Bartuli C, Valente T, Tului M. Plasma spray deposition and high temperature characterization of ZrB₂-SiC protective coatings. *Surf Coat Technol.* 2002;155(2-3):260-73.
16. Girin AG. Laws governing the fragmentation of a droplet in a high-speed stream. *J Eng Phys Thermophys.* 2011;84(5):1009-15.
17. Brenner AE, Peña AA, Phuah XL, Petorak C, Thompson B, Trice RW. Cyclic ablation of high-emissivity Sm-doped ZrB₂/SiC coatings on alumina substrates. *J Eur Ceram Soc.* 2018;38(4):1136-42.
18. Karlsdottir SN, Halloran JW, Henderson CE. Convection Patterns in Liquid Oxide Films on ZrB₂-SiC Composites Oxidized at a High Temperature. *J Am Ceram Soc.* 2007;90(9):2863-7.
19. Karlsdottir SN, Halloran JW. Formation of Oxide Films on ZrB₂-15 vol% SiC Composites During Oxidation: Evolution with Time and Temperature. *J Am Ceram Soc.* 2009;92(6):1328-32.
20. Hu P, Gui K, Yang Y, Dong S, Zhang X. Effect of SiC content on the ablation and oxidation behavior of ZrB₂-based ultra high temperature ceramic composites. *Materials.* 2013;6(5):1730-44.
21. Opila E, Levine S, Lorincz J. Oxidation of ZrB₂- and HfB₂-based ultra-high temperature ceramics: Effect of Ta additions. *J Mater Sci.* 2004;39(19):5969-77.
22. Ouyang G, Ray P, Kramer M, Akinc M. Effect of AlN substitutions on the oxidation behavior of ZrB₂-SiC composites at 1600°C. *J Am Ceram Soc.* 2016;99(10):3389-97.
23. Avdoshenko S, Strachan A. High-temperature emissivity of silica, zirconia and samaria from ab initio simulations: role of defects and disorder. *Model Simul Mat Sci Eng.* 2014;22[7]:075004.

How to cite this article: Peña AA, Vernon JP, Trice RW. Evaluation of rare-earth element dopants (Sm and Er) on ablation resistance of ZrB₂/SiC sintered-billets. *J Am Ceram Soc.* 2019;00:1-11. <https://doi.org/10.1111/jace.16422>